

Temporally-Consistent Koopman Autoencoders for Forecasting Dynamical Systems

Indranil Nayak^{1,2*}, Debdipta Goswami^{2,3}, Mrinal Kumar³,
Fernando Teixeira^{1,2}

¹ElectroScience Laboratory, The Ohio State University, Columbus,
43212, Ohio, USA.

²Department of Electrical and Computer Engineering, The Ohio State
University, Columbus, 43210, Ohio, USA.

³Department of Mechanical and Aerospace Engineering, The Ohio State
University, Columbus, 43210, Ohio, USA.

*Corresponding author(s). E-mail(s): nayak.77@osu.edu;

Abstract

Absence of sufficiently high-quality data often poses a key challenge in data-driven modeling of high-dimensional spatio-temporal dynamical systems. Koopman Autoencoders (KAEs) harness the expressivity of deep neural networks (DNNs), the dimension reduction capabilities of autoencoders, and the spectral properties of the Koopman operator to learn a reduced-order feature space with simpler, linear dynamics. However, the effectiveness of KAEs is hindered by limited and noisy training datasets, leading to poor generalizability. To address this, we introduce the Temporally-Consistent Koopman Autoencoder (tcKAE), designed to generate accurate long-term predictions even with constrained and noisy training data. This is achieved through a consistency regularization term that enforces prediction coherence across different time steps, thus enhancing the robustness and generalizability of tcKAE over existing models. We provide analytical justification for this approach based on Koopman spectral theory and empirically demonstrate tcKAE's superior performance over state-of-the-art KAE models across a variety of test cases, including simple pendulum oscillations, kinetic plasmas, fluid flows, and sea surface temperature data.

1 Introduction

Long-term forecasting sequential time-series data generated from a nonlinear dynamical system is a central problem in engineering. For classification or prediction of such time-series data, a precise analysis of the underlying dynamical system provides valuable insights to generate appropriate features and interpretability to any computational algorithm. This gives rise to a family of physics constrained learning (PCL) algorithms that incorporate constraints arising from physical consistency of the governing dynamical system.

Recently, a physics constrained approach for time-series learning based on Koopman methods [36] has been introduced. This approach uses an infinite-dimensional linear operator that encodes a nonlinear dynamics completely. The Koopman operator [25] provides a computationally preferable linear method to analyze and forecast dynamical systems. However, Koopman operator maps between infinite-dimensional function spaces, and hence, cannot be *in general* computationally represented without a finite-dimensional projection. Machine learning techniques utilize a finite-dimensional approximation of the Koopman operator by assuming the existence of a finite-dimensional Koopman invariant function space. This is usually achieved by an autoencoder network that maps the state-space into a latent space where the dynamics can be linearly approximated by the finite-dimensional Koopman operator encoded via a linear layer. This Koopman autoencoder (KAE) approach is attractive as it strikes a balance between the expressivity of deep neural networks and interpretability of PCL. Also, Koopman modal approximation can be readily used for stability analysis [28] and control [35, 18] of the underlying dynamical system in a data-driven fashion. Recent literature [7] also investigates the existence of a backward Koopman operator in order to impose an extra consistency constraint on the latent space linear map, giving rise to consistent Koopman autoencoder (cKAE) algorithm.

This manuscript proposes a new algorithm for consistent long-term prediction of time-series data generated from a nonlinear (possibly high-dimensional) dynamical system using a temporal consistency constraint with Koopman autoencoder framework. This algorithm, dubbed as temporally consistent Koopman autoencoder (tcKAE), compares the predictions from different initial time-instances to a final time in the *latent space*. This is in contrast with prior KAE methodologies, where the enforcement of multi-step look-ahead prediction loss is reliant on *labelled* data and latent space representation of the labelled data [7, 27, 40], a constraint when such data is scarce. The tcKAE is different since it evaluates predictions relative to each other, bypassing direct comparison with *labelled* data. This alleviates limitations on the maximum look-ahead step imposed by a limited training dataset. The tcKAE algorithm also differs from cKAE [7] in checking consistency because, unlike the latter, it does not require the existence of a backward dynamics. It is analytically shown that a KAE spanning a Koopman invariant subspace must satisfy the temporal consistency constraint and by enforcing it, tcKAE leads to higher expressivity and generalizability. This enforcement of temporal consistency in effect reduces the sensitivity of the KAE to noise, decreases the variance or uncertainty in future predictions and make it more robust with less training data as shown in the experiments. Consistency regularization have been used for semi-supervised learning in classification problems [37, 15, 16], but to the best of

our knowledge, this is the first attempt to regularize multi-step temporal consistency for dynamical system learning.

2 Background

2.1 Related work

Recurrent neural networks: The idea of forecasting dynamical systems using neural networks, particularly using recurrent neural networks (RNNs), dates back to several decades [8, 4]. Recent advances in big data, machine learning algorithms and computational hardware, have rekindled the interest in this domain. Emergence of innovative architectures such as Long Short-Term Memory (LSTM) [20], or gated neural networks (GRUs) [13] have enhanced the prediction capabilities of NN models significantly. However, training an RNN is fraught with vanishing and exploding gradient problems [9] which can be solved by approaches like analyzing stability [29] or using unitary hidden weight matrices [3]. But these can affect the short term modeling capability by reducing the expressivity of the RNNs [23]. Another drawback of RNNs is the lack of generalizability and interpretability especially when used for predicting a physical system. To make RNN physically consistent, a number of methods are presented to take physical constraints into account. These range from making a physics guided architecture [22], relating it to dynamical systems [39] or differential equations [11]. Hamiltonian neural networks [19] aims to learn the conserved Hamiltonian as a physical constraint but works only for lossless systems. In this paper, we use the linear operator-based recurrent architecture along with a physical prediction constraint to develop a more generalizable prediction model.

Koopman-based methods: The Koopman operator-based approach exploits the linearity [36] in an infinite dimensional function space to yield a linearly recurrent prediction scheme. A number of non-neural dictionary-based approach relying on the dynamic mode decomposition (DMD) [38] are proposed [42, 41, 35, 17, 18]. However, these methods implicitly assumes a dictionary spanning a Koopman invariant subspace. Neural approaches using Koopman autoencoder (KAE) provides a better alternative to define a Koopman invariant function space where the dynamics can be linearly approximated [40, 34, 27]. [26] showcased the superiority of Koopman-based spectral methods over LSTM, Gated Recurrent Unit (GRU), and Echo State Networks (ESNs) due its ability to extract "slow" frequencies which can have significant effect for the long-term predictions. Furthermore, the autoencoder architecture is particularly well-suited (order reduction) for modeling high-dimensional physical systems, the primary goal of this work. However, most of the KAE models just focus on multi-step prediction errors and without any test on consistency of predictions. Recent work [7] on backward Koopman operator provides a consistency test by making the predictions forward and backward consistent, but works only when a backward dynamics is well-defined.

2.2 Koopman theory: an overview

Consider a discrete-time dynamical system on a N_d -dimensional compact manifold \mathcal{M} , evolving according to the flow-map $\mathbf{f} : \mathcal{M} \mapsto \mathcal{M}$:

$$\mathbf{x}_{n+1} = \mathbf{f}(\mathbf{x}_n), \quad \mathbf{x}_n \in \mathcal{M}, \quad n \in \mathbb{N} \cup \{0\}. \quad (1)$$

Let \mathcal{F} be a Banach space of complex-valued observables $\psi : \mathcal{M} \rightarrow \mathbb{C}$. The discrete-time *Koopman operator* $\mathcal{K} : \mathcal{F} \rightarrow \mathcal{F}$ is defined as

$$\mathcal{K}\psi(\cdot) = \psi \circ \mathbf{f}(\cdot), \quad \text{with } \psi(\mathbf{x}_{n+1}) = \mathcal{K}\psi(\mathbf{x}_n) \quad (2)$$

where \mathcal{K} is infinite-dimensional, and linear over its argument. The scalar observables ψ are referred to as the Koopman observables. Koopman eigenfunctions ϕ are special set of Koopman observables that satisfy $(\mathcal{K}\phi)(\cdot) = \lambda\phi(\cdot)$, with an eigenvalue λ . Considering the Koopman eigenfunctions span the Koopman observables, a vector valued observable $\mathbf{g} \in \mathcal{F}^p = [\psi_1 \ \psi_2 \ \dots \ \psi_p]^\top$ can be expressed as a sum of Koopman eigenfunctions $\mathbf{g}(\cdot) = \sum_{i=1}^{\infty} \phi_i(\cdot) \mathbf{v}_i^{\mathbf{g}}$, where $\mathbf{v}_i^{\mathbf{g}} \in \mathbb{R}^p, i = 1, 2, \dots$, are called the *Koopman modes* of the observable $\mathbf{g}(\cdot)$. This modal decomposition provides the growth/decay rate $|\lambda_i|$ and frequency $\angle \lambda_i$ of different Koopman modes via its time evolution

$$\mathbf{g}(\mathbf{x}_t) = \sum_{i=1}^{\infty} \lambda_i^t \phi_i(\mathbf{x}_0) \mathbf{v}_i^{\mathbf{g}}. \quad (3)$$

The Koopman eigenvalues and eigenfunctions are properties of the dynamics only, whereas the Koopman modes depend on the observable.

Koopman modes can be analyzed to understand the dominant characteristics of a complex dynamical system and getting traction in fluid mechanics [36], plasma dynamics [32], control systems [35], unmanned aircraft systems [31], and traffic prediction [5]. In addition, it is also being used for machine learning tasks and training deep neural networks [14]. Several methods have also been developed to compute the Koopman modal decomposition, e.g., DMD and EDMD [38, 42], Ulam-Galerkin methods, and deep neural networks [34, 43]. In this paper, we primarily focus on long-term prediction of autonomous dynamical systems using Koopman modes with autoencoder networks.

3 Method

3.1 Prediction via Koopman invariant subspace: Koopman autoencoders (KAE)

Koopman operator, being an infinite-dimensional one, must be projected onto a finite-dimensional basis for any practical prediction algorithm. The equation in (3) can be truncated to finite set of terms in the presence of a finite-dimensional Koopman invariant subspace. However, discovering such finite-dimensional Koopman invariant subspaces purely from data is a challenging task, and an active area of research. Recent works [40, 27, 34] leverage the nonlinear function approximation capabilities of neural

networks to find a suitable transformation from the state space \mathcal{M} to a Koopman invariant subspace via a latent state (\mathbf{z}). These models are encompassed within the broader umbrella of Koopman autoencoders (KAE) which strives to find a suitable transformation from state space to the Koopman observable space where the dynamics is linear, and can be easily learned. The basic operation of KAE can be decomposed into three components (4), *i*) encoding ($\Psi_e(\cdot)$) : $\mathcal{M} \rightarrow \mathbb{R}^{N_l}$ that transforms the original state \mathbf{x} to a Koopman observable $\mathbf{z} \in \mathbb{R}^{N_l}$, *ii*) advancing the dynamics in that transformed space through a linear operator ($K \in \mathbb{R}^{N_l \times N_l}$), and *iii*) decoding ($\Psi_d(\cdot)$) back to the original state space:

$$\mathbf{z}_n \approx \Psi_e(\mathbf{x}_n) \quad \rightarrow \quad \mathbf{z}_{n+k} = K^k \cdot \mathbf{z}_n \quad \rightarrow \quad \mathbf{x}_{n+k} \approx \Psi_d(\mathbf{z}_{n+k}) = \hat{\mathbf{x}}_{n+k}, \quad (4)$$

where K is the finite-dimensional restriction of \mathcal{K} , which advances \mathbf{z} by k time-steps (or time samples), and $\hat{\mathbf{x}}$ denotes the KAE reconstruction of the state. Note that for traditional autoencoders the encoding operation typically result in dimensionality reduction which is beneficial when dealing with high-dimensional dynamical systems. Traditionally, since we are mostly interested in future prediction of the state, KAE is trained by minimizing the difference between $\hat{\mathbf{x}}_{n+k}$ and \mathbf{x}_{n+k} , with $k \in \mathbb{Z}_+ \cup \{0\}$. The loss functions traditionally used for training KAEs are the identity loss \mathcal{L}_{id} ($k = 0$), and the forward loss L_{fwd} ($k = 1, 2, \dots$) [7].

$$\mathcal{L}_{id} = \frac{1}{2M} \sum_{n=1}^M \|\hat{\mathbf{x}}_n - \mathbf{x}_n\|_2, \quad \mathcal{L}_{fwd} = \frac{1}{2k_m M} \sum_{k=1}^{k_m} \sum_{n=1}^M \|\hat{\mathbf{x}}_{n+k} - \mathbf{x}_{n+k}\|_2^2, \quad (5)$$

where $\|\cdot\|_2$ is the 2-norm, M is the number of samples over which we want to enforce the loss, and k_m is the maximum value of k , i.e. the maximum look-ahead step for multi-step training. Recent work in [7] demonstrated that including backward dynamics ($K_b \in \mathbb{R}^{N_l \times N_l}$) leads to better stability resulting in more accurate long-term predictions. The idea is to incorporate a backward loss term (\mathcal{L}_{bwd}) with forward-backward consistency loss (\mathcal{L}_{con}),

$$\mathcal{L}_{bwd} = \frac{1}{2k_m M} \sum_{k=1}^{k_m} \sum_{n=1}^l \|\hat{\mathbf{x}}_{n-k} - \mathbf{x}_{n-k}\|_2^2 \quad (6)$$

$$\mathcal{L}_{con} = \sum_{i=1}^{N_b} \frac{1}{2i} \|K_{bi^*} K_{*i} - I_{N_l}\|_F + \frac{1}{2i} \|K_{*i} K_{bi^*} - I_{N_l}\|_F, \quad (7)$$

where N_l is the latent space dimension, K_{bi^*} is the upper i rows of K_b , K_{*i} is the i left most columns of K , $\|\cdot\|_F$ denotes the Frobenius norm, and $I_{N_l} \in \mathbb{R}^{N_l \times N_l}$ is the identity matrix of dimension $N_l \times N_l$.

3.2 Prediction-consistent Koopman autoencoder (tcKAE)

In this section, we describe our proposed temporally-consistent Koopman autoencoder (tcKAE) architecture. The key idea is to introduce a consistency regularization term for

training KAE in order to enforce consistency among future predictions. The fundamental idea derives from the time-invariance property of the autonomous dynamical systems. In the context of (1), the temporal consistency can be stated as the direct result of the following:

$$\mathbf{f}^\kappa(\mathbf{x}_n) = \mathbf{f}^{\kappa+k}(\mathbf{x}_{n-k}), \quad \forall n, \kappa \in \mathbb{Z}_+ \cup \{0\}, \quad k = 1, 2, \dots, n, \quad (8)$$

where $\mathbf{f}^\kappa = \mathbf{f} \circ \mathbf{f} \circ \dots (\kappa \text{ times}) \dots \circ \mathbf{f}$, with \circ being the composition operator. One key aspect of our approach is that instead of enforcing this consistency in the original state space, we do so in the Koopman invariant subspace (latent space). This helps avoid computation in the high-dimensional space, as well as provide robustness to noise. We justify enforcing such consistency in the latent space by summarizing the desired property of a consistent autoencoder Ψ_e and constructing the architecture of this framework. The autoencoder $\Psi_e(\cdot) = [\psi_1(\cdot), \dots, \psi_{N_l}(\cdot)]$ defines a vector valued observable of the state space \mathcal{M} where each ψ_i is a scalar valued function. Let \mathcal{G} be the span of $\{\psi_1, \dots, \psi_l\}$. In order for the linear recurrent matrix K to asymptotically approximate the projection of Koopman operator \mathcal{K} on \mathcal{G} , the latter needs to be Koopman invariant, i.e., $\mathcal{K}\mathcal{G} \subset \mathcal{G}$. The Koopman invariance will ensure the linear recurrent structure

$$\hat{\mathbf{x}}_{n+1} = \Psi_d \circ K \circ \Psi_e(\mathbf{x}_n). \quad (9)$$

The proposed architecture introduces a multi-step temporal consistency loss (not against labelled data) in the latent space in order to strengthen the Koopman invariance of the latent function space \mathcal{G} . In the following, we summarize the desirable temporal consistency of the encoder functions upon which the proposed method is constructed.

Theorem 1. *Let $\Psi_e(\cdot) = [\psi_1(\cdot), \dots, \psi_{N_l}(\cdot)]^T \in \mathcal{F}^{N_l}$ denotes a vector valued function comprised with scalar functions $\psi_i(\cdot) \in \mathcal{F}$. The latent function space $\mathcal{G} = \{\psi_1(\cdot), \dots, \psi_{N_l}(\cdot)\}$ forms a Koopman invariant subspace with respect to the system dynamics (1) if and only if there exists $K \in \mathbb{R}^{N_l \times N_l}$ such that*

$$\Psi_e(\mathbf{x}_{n+\kappa}) = K^\kappa \Psi_e(\mathbf{x}_n) \quad (10)$$

for all $n \geq 0$ and $\kappa \geq 1$.

Proof. (\Rightarrow) Suppose $\Psi_e(\cdot)$ is such defined that $\text{span}(\mathcal{G})$ is a Koopman invariant subspace. We prove this part via induction. For any $n \geq 0$, (10) is trivially satisfied for $\kappa = 1$ with some matrix K . Now suppose it is satisfied for a fixed $\kappa \in \mathbb{N}$. Then, $\Psi_e(\mathbf{x}_{n+\kappa+1}) = \Psi_e \circ \mathbf{f}(\mathbf{x}_{n+\kappa}) = \mathcal{K}\Psi_e(\mathbf{x}_{n+\kappa}) = \mathcal{K}K^\kappa \Psi_e(\mathbf{x}_n) = K^\kappa \mathcal{K}\Psi_e(\mathbf{x}_n) = K^\kappa \Psi_e \circ \mathbf{f}(\mathbf{x}_n) = K^\kappa \Psi_e(\mathbf{x}_{n+1}) = K^{\kappa+1} \Psi_e(\mathbf{x}_n)$, where the first two steps are by the definition of Koopman operator, next two steps are by the linearity of the same, and the last step is by the induction anchor.

(\Leftarrow) Suppose $\exists K \in \mathbb{R}^{N_l \times N_l}$ such that (10) is satisfied for all $n \geq 0$ and $\kappa \geq 1$. Then it must be satisfied for $n = 0$ and $\kappa = 1$, i.e., $\Psi_e(\mathbf{x}_1) = K\Psi_e(\mathbf{x}_0)$. Since \mathbf{x}_0 can be anything in \mathcal{M} , this yields $\Psi_e \circ \mathbf{f}(\mathbf{x}) = K\Psi_e(\mathbf{x})$ for all $\mathbf{x} \in \mathcal{M}$, i.e., $\Psi_e \circ \mathbf{f}(\cdot) = K\Psi_e(\cdot)$. Let $g \in \text{span}(\mathcal{G})$ be an observable. Then, $\exists \alpha \in \mathbb{R}^l$ such that $g(\cdot) = \alpha^T \Psi_e(\cdot)$. Now, $\mathcal{K}g(\cdot) = g \circ \mathbf{f}(\cdot) = \alpha^T \Psi_e \circ \mathbf{f}(\cdot) = \alpha^T K\Psi_e(\cdot)$, i.e., $\mathcal{K}g \in \text{span}(\mathcal{G})$. Hence, $\text{span}(\mathcal{G})$ forms a Koopman invariant subspace. \square

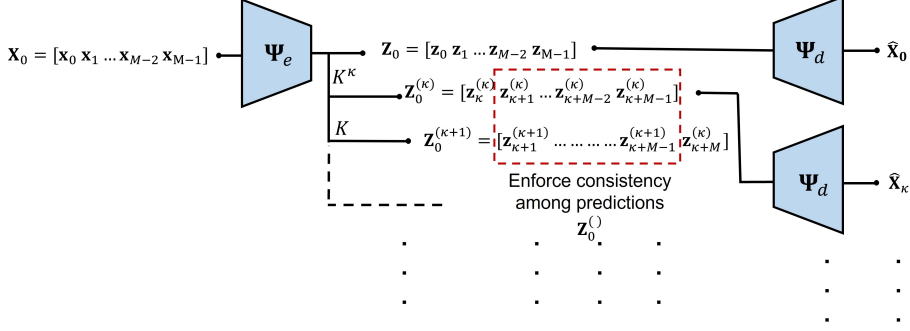


Fig. 1 Illustration of enforcement of temporal consistency among predictions in Koopman invariant latent space.

Theorem 1 ensures that, in the latent space, encoded state at any time instant must be equal to the encoded state of any previous time multiplied with K^κ where κ denotes the time-step between those two instances. It also forces the latent state to have linear time invariant dynamics with a constant state-transition matrix K . Theorem 1 provides a method to ensure the autoencoder span a Koopman invariant subspace by enforcing temporal consistency as follows.

Corollary 1. For a KAE $\Psi_e : \mathcal{M} \rightarrow \mathbb{R}^{N_l}$, if the associated function space \mathcal{G} is Koopman invariant, then for any $n \geq 0$ and $\kappa \geq 1$, $K^{\kappa-p} \Psi_e(\mathbf{x}_{n+p}) = K^{\kappa-q} \Psi_e(\mathbf{x}_{n+q})$ for all $p, q = 1, \dots, \kappa - 1$, i.e.,

$$K^{\kappa-1} \Psi_e(\mathbf{x}_{n+1}) = K^{\kappa-2} \Psi_e(\mathbf{x}_{n+2}) = \dots (p \neq q)$$

Corollary 1 is essentially heart of the temporal consistency loss. In order to define our loss function, let us consider the reference time-step to be n . For a batch size of M (in latent space $\mathbf{Z}_n = [\mathbf{z}_n \ \mathbf{z}_{n+1} \ \dots \ \mathbf{z}_{n+M-1}]$), let the KAE advance the dynamics up to κ_m time-steps, giving rise to a set of batches $\mathbf{Z}_n^{(\kappa)} = [\mathbf{z}_{n+\kappa}^{(\kappa)} \ \mathbf{z}_{n+1+\kappa}^{(\kappa)} \ \dots \ \mathbf{z}_{n+M+\kappa-1}^{(\kappa)}]$ with $\kappa = 1, 2, \dots, \kappa_m$, where the superscript (κ) denotes the number of operations of K . The consistency loss \mathcal{L}_{tc} (Fig. 1) can be defined as,

$$\mathcal{L}_{tc} = \frac{1}{2\kappa_m} \sum_{\kappa=1}^{\kappa_m} \mathcal{L}_\kappa, \quad \mathcal{L}_\kappa = \frac{1}{(M-1)} \sum_{p=1}^{M-1} \frac{1}{p} \sum_{q=1}^p \|\mathbf{z}_{n+\kappa+p}^{(\kappa)} - \mathbf{z}_{n+\kappa+p}^{(\kappa+q)}\|_2^2. \quad (11)$$

The total loss (\mathcal{L}_{tot}) for training tKAE is given by,

$$\mathcal{L}_{tot} = \gamma_{id} \mathcal{L}_{id} + \gamma_{fwd} \mathcal{L}_{fwd} + \gamma_{bwd} \mathcal{L}_{bwd} + \gamma_{con} \mathcal{L}_{con} + \gamma_{tc} \mathcal{L}_{tc}, \quad (12)$$

Where γ_{id} , γ_{fwd} , γ_{bwd} , γ_{con} and γ_{tc} are the corresponding weights.

Remark 1. The temporal consistency loss enforces a Koopman invariant subspace by virtue of the time-homogeneity of the latent-state dynamics, i.e., the Koopman operator is time-invariant for an autonomous system. This provides a physics constrained learning method for dynamical system prediction even from a smaller dataset.

3.3 Baseline

The performance of the proposed prediction-consistent Koopman autoencoder (tcKAE) is compared against the state-of-the-art KAE models forecasting models for physical systems. As discussed earlier, several neural-network based models such as recurrent neural networks (RNNs) [13, 24, 11], Hamiltonian neural networks (HNNs) [19] have already been applied successfully in forecasting dynamical systems. However, these models do not fare well for very long-term predictions [26]. Koopman-based autoencoder models [27, 34] have been shown to be effective in capturing this long-term behavior, especially for high-dimensional systems. However, recently proposed consistent Koopman autoencoder [7] which we will refer to as cKAE, has been shown to outperform all the mentioned methods for long-term predictions in terms of stability. We will consider cKAE as the baseline for benchmarking our proposed tcKAE for several datasets. We will also compare our results with dynamic autoencoders (DAEs) term used in [7] to describe [27, 34] with $\gamma_{\text{bwd}} = \gamma_{\text{con}} = 0$.

3.4 Datasets

In order to streamline the discussion, we adopt the following notation: the complete dataset is denoted by $\mathbf{X} \in \mathbb{R}^{N_{\text{dim}} \times N_{\text{tot}}}$, where N_{dim} is the dimension of the state-space, and N_{tot} is the total number of time samples. We denote the training set as $\mathbf{X}_{\text{train}} \in \mathbb{R}^{N_{\text{dim}} \times N_{\text{train}}}$ and testing set as $\mathbf{X}_{\text{test}} \in \mathbb{R}^{N_{\text{dim}} \times N_{\text{test}}}$ with N_{train} and N_{test} being the number of time samples in training and testing set respectively.

3.4.1 Undamped Pendulum:

The undamped pendulum is a classic textbook example of nonlinear dynamical system for benchmarking performance of data-driven predictive models [7, 19, 12, 10, 6]. Although, the pendulum dynamics do not fall under typical PDE-governed high-dimensional systems, it serves as an excellent illustrative example due to the wide range of physical systems they represent, ranging from orbital mechanics, microwave cavities to select biological and quantum systems. We use the elliptical functions [7, 1] for exact solution of the motion governed by the ODE $\frac{d^2\theta}{dt^2} + \frac{g}{l}\sin\theta = 0$, where $\theta \in [0, 2\pi]$ denotes the angular displacement from equilibrium $\theta = 0$ in radians. The gravitational constant and length of the pendulum is denoted by g and l respectively. We consider $g = 9.8 \text{ m/s}^2$, and $l = 1 \text{ m}$ with initial condition $\theta = \theta_0$ and $\frac{d\theta}{dt} = \dot{\theta} = 0$. We sample the solution at interval of 0.1 s upto 220 s, resulting in the dataset $\Theta \in \mathbb{R}^{2 \times 2200}$ with 2200 time samples. Note that the dimensionality of the state-space is two, since we have two states θ and $\dot{\theta}$. In order to mimic a high-dimensional system, we use a random orthogonal transformation [7] to rotate it to higher dimensional ($N_{\text{dim}} = 64$) space, i.e. $\mathbf{X} = \mathbf{P} \cdot \Theta$, where $\mathbf{P} \in \mathbb{R}^{64 \times 2}$ is a random orthogonal matrix. The final dataset $\mathbf{X} \in \mathbb{R}^{64 \times 2200}$ consists of 2200 time samples of a state with dimension 64.

3.4.2 Oscillating electron beam

Plasma systems are excellent candidates for data-driven modeling due to their high-dimensionality, and inherent nonlinearity arising from the complex wave-particle

interaction. A two dimensional electron beam oscillating under the influence of an external transverse magnetic flux is simulated using charge-conserving electromagnetic particle-in-cell (EMPIC) algorithm [30]. The solution domain ($1 \text{ m} \times 1 \text{ m}$) is discretized using unstructured triangular mesh with 844 nodes, 2447 edges, and 1604 elements (triangles). The electric field data ($\mathbf{e} \in \mathbb{R}^{2447}$) is sampled at every 0.32 ns. Starting from 80 ns, total 1751 time samples are collected with the complete dataset $\mathbf{X} \in \mathbb{R}^{2447 \times 1751}$. More details regarding data generation are provided in the Appendix A.

3.4.3 Flow past cylinder

Flow past cylinder is another common dynamical system used for benchmarking data-driven models. The simulation was carried out using MATLAB’s FEAtool. A cylinder with diameter 0.1 m is located at a height of 0.2 m. The fluid is characterized by its density $\rho = 1 \text{ Kg/m}^3$, and dynamic viscosity $\mu = 0.001 \text{ Kg/m s}$. The flow is unsteady with a maximum velocity of 1 m/s and mean velocity $\frac{2}{3}$ of the maximum velocity. The simulation is run for 80 s until the steady state is achieved, and the horizontal u component of the velocity is probed at every 0.02 s starting from 20 s. The complete dataset $\mathbf{X} \in \mathbb{R}^{2647 \times 3001}$ consists of 3001 time samples. More details regarding the simulation setup can be found in Appendix A.

3.4.4 Sea Surface Temperature (SST)

The monthly variation of SST was taken from [21, 2]. We use the dataset "/Dataset-s/noaa.oisst.v2.highres/sst.mon.mean.nc" which accounts for monthly values from 1981/09 to 2023/08. We take every 10th sample of latitude and longitude for modeling. Additionally, the dataset was preprocessed to remove anomalous values and instances containing 'NaN'. Since the measurement data already contains noise, we test our method for different training dataset size. The complete dataset $\mathbf{X} \in \mathbb{R}^{6822 \times 503}$ consists of total 503 time samples. The training strategy is same for the rest of the datasets in the original manuscript.

3.5 Training strategy

We follow the training strategy as in [7, 1]. We partition the dataset \mathbf{X} into training ($\mathbf{X}_{\text{train}}$) and testing (\mathbf{X}_{test}) set. Guided by one of the core motivations of this paper to analyze the cases with limited data, we analyze three different scenarios for each dataset with three different values of N_{train} . Since we are using the consistent Koopman autoencoder (cKAE) [7] for benchmarking, we perform the hyperparameter search to get best possible performance for cKAE. We then maintain those optimal hyperparameters for cKAE and introduce our proposed loss \mathcal{L}_{tc} . We tune three additional hyperparameters for the proposed tcKAE, namely the weight γ_{tc} corresponding to \mathcal{L}_{tc} , the maximum look-ahead step κ_m , and the epoch (e_s) for switching to non-zero γ_{tc} . Up to e_s we train without enforcing the consistency regularization, and switch to nonzero γ_{tc} from e_s onward. We also observe the effect of noise on model performance for two different noise level, 30 dB and 40 dB (zero mean Gaussian). For different level of noise we tune the weights of different loss components to get best possible accuracy keeping other parameters fixed. For the pendulum, we analyze the effect of noise for

all three different values N_{train} , whereas for high-dimensional fluid flow and plasma system we analyze the effect of noise for the largest value of N_{train} . Note that for DAE, we tune the hyperparameters from scratch to obtain best possible performance. The detailed training parameters along with the network architecture are provided in the supplementary material.

The generalizability of the models are assessed by its performance on the test set for long-term predictions. The evaluation of the model’s performance is based on the relative 2-norm error denoted by, $\delta_n = \frac{\|\hat{\mathbf{x}}_n - \mathbf{x}_n\|_2}{\|\mathbf{x}_n\|_2}$, averaged over prediction region, and variance in the predicted values. The variance is quantified by the 90% confidence interval, defined by the 5th and 95th percentiles of the error, providing a robust summary of the typical error range by excluding the extreme 5% of values at both ends of the distribution. Note that for notational conciseness we provide the width of the 90% interval indicating degree of variance. Note that since we are dealing with time-series, the sequential integrity of the samples in $\mathbf{X}_{\text{train}}$ and \mathbf{X}_{test} are preserved. First 30 samples from \mathbf{X}_{test} are fed to the pre-trained models to reconstruct the entire trajectory spanning \mathbf{X}_{test} , which is then compared against the noise-free ground truth to evaluate its performance. The variation in error for multiple inputs also helps assess the robustness of the model.

4 Results

4.1 Undamped pendulum

We generate the data using the initial condition $\theta_0 = 0.8$, $\dot{\theta} = 0$. One cycle of oscillation is covered approximately by 20 time-steps. We perform the tests for $N_{\text{train}} = 32, 50$ and 90, with two different noise levels 40 dB and 30 dB for each N_{train} . The relative 2-norm error is calculated over 1900 time-samples in testing set (extrapolation region). The results are summarized in Table 1 and Table 2.

Table 1 Error (%) comparison: DAE, cKAE, and tcKAE on clean pendulum data. The quantities inside parenthesis show the width of 90% confidence interval.

Method	$N_{\text{train}} = 32$	$N_{\text{train}} = 50$	$N_{\text{train}} = 90$
DAE	26.733 (90.11)	12.119 (43.23)	11.287 (42.34)
cKAE	9.684 (33.00)	5.914 (14.52)	4.578 (21.20)
tcKAE	2.936 (9.20)	3.131 (5.81)	3.059 (13.00)

As can be seen in Table 1, our proposed tcKAE has clear advantage over DAE or cKAE for clean data. This advantage is magnified for $N_{\text{train}} = 32$, which covers approximately one and half cycle of oscillation of the pendulum. The advantage tends to diminish with increasing size of training set. Large N_{train} essentially makes learning with larger look-ahead step κ possible for labelled training data, resulting in enhanced stability for long-term predictions for DAE and cKAE. Table 1 also shows that the variation of error (values inside parenthesis) is lowest for tcKAE. We see a similar trend with respect to N_{train} when noise is included. However, interestingly with addition of

Table 2 Error (%) comparison for different N_{train} and noise levels for pendulum data.

Method	40 dB SNR			30 dB SNR		
	$N_{\text{train}} = 32$	$N_{\text{train}} = 50$	$N_{\text{train}} = 90$	$N_{\text{train}} = 32$	$N_{\text{train}} = 50$	$N_{\text{train}} = 90$
DAE	32.237 (127.65)	8.364 (22.03)	9.336 (36.58)	38.292 (178.52)	10.533 (35.64)	11.466 (45.71)
cKAE	9.440 (36.27)	5.999 (14.19)	6.588 (41.96)	17.733 (77.04)	6.863 (23.02)	7.684 (32.07)
tcKAE	4.018 (15.13)	3.832 (8.00)	3.259 (16.00)	12.500 (49.70)	5.494 (15.56)	6.104 (23.20)

noise in some cases the relative error actually decreases. This should not be surprising since models tend to overfit with limited data, and adding noise is one of the solutions to avoid overfitting. Overall, tcKAE provides more accurate estimate of the state for long-term prediction.

4.2 Oscillating Electron Beam

For the electron beam oscillation, one period approximately comprises of 25 time samples. In order to assess the performance of the Koopman models for limited dataset, we train the models for $N_{\text{train}} = 40, 50$ and 100. For clean data (Table 3), tcKAE performs along the expected line with increase size of training dataset. Since tcKAE seems to have obvious advantage for limited dataset, we only focus on the large dataset ($N_{\text{train}} = 100$) in order to assess the effect of noise. For different noise levels tcKAE fails to provide any significant advantage, indicating that primary advantage of tcKAE lies in handling limited dataset.

Table 3 Results for electron beam oscillation: Error (%) comparison between DAE, cKAE, and tcKAE for clean data (left); for $N_{\text{train}} = 100$ and noisy data (right).

Method	$N_{\text{train}} = 40$	$N_{\text{train}} = 50$	$N_{\text{train}} = 100$	Method	Clean	40 dB SNR	30 dB SNR
DAE	7.713 (11.07)	2.964 (4.32)	0.770 (0.94)	DAE	0.770 (0.94)	1.372 (0.75)	3.847 (1.68)
cKAE	7.559 (10.19)	2.468 (2.50)	0.811 (0.93)	cKAE	0.811 (0.93)	1.359 (0.73)	3.640 (1.05)
tcKAE	2.802 (2.15)	1.754 (0.85)	0.802 (0.90)	tcKAE	0.802 (0.90)	1.335 (0.65)	3.560 (0.84)

4.3 Flow Past Cylinder

Table 4 Results for flow past cylinder: error (%) comparison between DAE, cKAE, and tcKAE for clean data (left); for $N_{\text{train}} = 120$ and noisy data (right)

Method	$N_{\text{train}} = 40$	$N_{\text{train}} = 50$	$N_{\text{train}} = 120$	Method	Clean	40 dB SNR	30 dB SNR
DAE	1.405 (2.84)	0.413 (0.58)	0.062 (0.06)	DAE	0.062 (0.06)	0.635 (0.85)	3.211 (5.27)
cKAE	2.220 (5.39)	0.398 (0.59)	0.064 (0.06)	cKAE	0.064 (0.06)	0.555 (0.61)	9.4887 (21.53)
tcKAE	1.162 (2.477)	0.375 (0.53)	0.061 (0.04)	tcKAE	0.061 (0.04)	0.484 (0.44)	1.745 (1.62)

In case of flow past cylinder, since one cycle approximately contains 30 time samples, we consider $N_{\text{train}} = 40, 50$ and 120. Model performance is tested against different noise levels for $N_{\text{train}} = 120$. The final error is calculated by averaging the 2-norm relative error over 2500 prediction steps beyond the training region. This example is interesting since even for limited data all of the models show good accuracy (Table 4). However, in presence of noise tcKAE outperforms both DAE and cKAE. Note that the absurdly high value for cKAE for 30 dB SNR is most likely an outlier.

4.4 Sea Surface Temperature

For the SST data we compare tcKAE only with cKAE for three different training dataset sizes. Interestingly, for SST data the advantage of tcKAE is not very obvious, which points out one of the limitations of tcKAE, the inherent assumption of time-invariance. SST variations are generally not time-invariant due to the impact of multiple time-varying factors, such as atmospheric conditions, ocean currents, and longer-term climate patterns. The inherent dynamics of SSTs are influenced by both periodic seasonal changes and non-periodic variations such as El Niño and La Niña events [33], which can inject anomalies in the SST variation.

Table 5 Error (%) comparison between cKAE and tcKAE for SST

Method	$N_{\text{train}} = 32$	$N_{\text{train}} = 60$	$N_{\text{train}} = 120$
cKAE	6.361 (12.67)	4.444 (7.11)	4.088 (6.14)
tcKAE	6.310 (12.36)	4.381 (6.73)	3.960 (5.84)

Table 6 Ablation study for oscillating electron beam

	γ_{id}	γ_{fwd}	γ_{bwd}	γ_{con}	γ_{tc}	Average relative error(%)
$N_{\text{train}} = 40$, clean	1	0.5	0	0	0	7.713
	1	0.5	0	0	1e-1	3.084
	1	0.5	1e-3	1e-5	0	7.559
	1	0.5	1e-3	1e-5	1e-1	2.802
$N_{\text{train}} = 100$, clean	1	0.01	0	0	0	0.771
	1	0.01	0	0	1e-3	0.725
	1	0.05	1e-1	1e-5	0	0.811
	1	0.05	1e-1	1e-5	1e-3	0.802
$N_{\text{train}} = 100$, 30 dB noise	1	0.01	0	0	0	3.847
	1	0.01	0	0	1e-2	3.574
	1	0.1	1e-1	1e-5	0	3.640
	1	0.1	1e-1	1e-5	1e-2	3.560

5 Conclusion

In this paper, we proposed a physics constrained learning (PCL) model named prediction-consistent Koopman autoencoder (tcKAE) which are Koopman autoencoders (KAE) with a

temporal consistency test for forecasting time-series data from nonlinear complex systems. The key approach uses the time-invariance property of the Koopman operator for autonomous dynamical systems to enforce temporal consistency in the latent variables. The tcKAE is evaluated on four datasets and compared against other KAE techniques including the most recent cKAE [7]. It outperforms the state-of-the-art methods for shorter training length and noisy training data, but have limited advantage when data is abundant or the underlying dynamics is time-variant. The ability of tcKAE to handle limited data can be crucial since simulation of high-dimensional physical system can often be computationally demanding. This method can be extended to non-autonomous control systems with a bilinearly recurrent KAE architecture by using the bilinear structure proposed in [18].

Acknowledgments. This work was funded in part by the Department of Energy Grant DE-SC0022982 through the NSF/DOE Partnership in Basic Plasma Science and Engineering and in part by the Ohio Supercomputer Center Grant PAS-0061.

Appendix A Simulation Setup

In this section we discuss the simulation setup in details for both the oscillating electron beam and flow past cylinder.

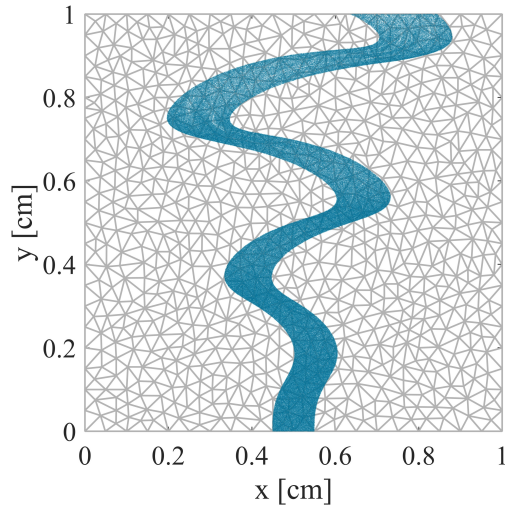


Fig. A1 Snapshot of electron beam at $t = 8$ ns.

A.1 Oscillating electron beam

A two-dimensional (2-D) electron beam (Fig. A1) is simulated inside a square cavity of dimension $1 \text{ cm} \times 1 \text{ cm}$ using a charge-conserving electromagnetic particle-in-cell (EMPIC) algorithm [30]. The electron beam is propagating along the +ve y direction under the influence of an oscillating transverse magnetic flux. The solution domain is discretized using irregular triangular mesh (grey lines in Fig. A1) with $N_0 = 844$ nodes, $N_1 = 2447$ edges and $N_2 = 1604$ elements (triangles). The blue dots in Fig. A1 represent the superparticles which are discretized

representation of the phase-space of electrons (delta distribution in both position and velocity). The superparticles are essentially the point charges with charge $q_{sp} = r_{sp}q_e$, and mass $m_{sp} = r_{sp}m_e$, where r_{sp} is the superparticle ratio with q_e and m_e respectively representing the charge and mass of an electron. We select $r_{sp} = 5000$. The superparticles are injected from the bottom of the cavity randomly with uniform distribution over the region $[0.45 \text{ cm}, 0.55 \text{ cm}]$ with the injection rate of 50 superparticles per time-step. The superparticles are injected along the vertical direction with $v_y = 5 \times 10^6 \text{ m/s}$. The external oscillating magnetic flux can be represented by $\mathcal{B}_{ext} = \mathcal{B}_0 \sin(2\pi/T_{osc}) \hat{z}$ with $\mathcal{B}_0 = 2.5 \times 10^{-2} \text{ T}$, and $T_{osc} = 0.8 \text{ ns}$. The time-step for the EMPIC simulation is taken to be $\Delta t = 0.2 \text{ ps}$.

A.2 Flow past cylinder

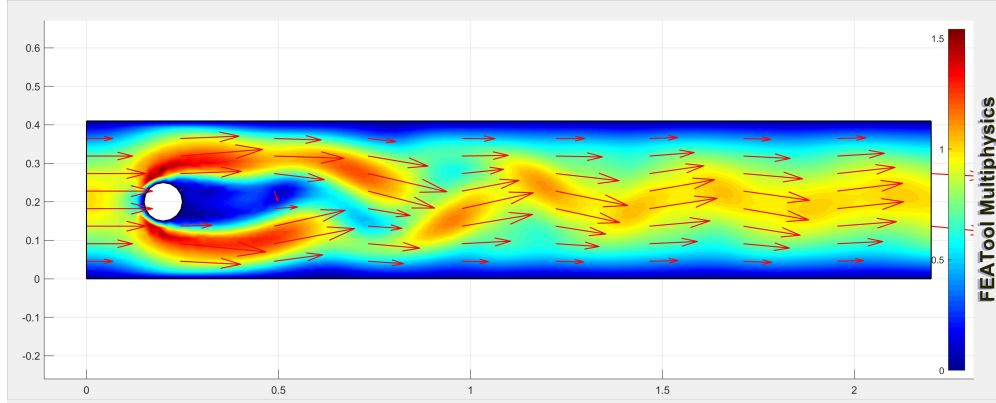


Fig. A2 Snapshot of velocity field at $t = 80 \text{ s}$.

The whole simulation setup is shown in Fig. A2. The 2-D solution domain ($2.2 \text{ m} \times 0.41 \text{ m}$) is discretized using irregular triangular mesh with number of nodes $N_0 = 2647$, and number of elements (triangles) $N_2 = 5016$. The cylinder has the diameter of 0.1 m with center of the cylinder located at $(0.2 \text{ m}, 0.2 \text{ m})$. The flow is assumed to be incompressible, and governed by the Navier-Stokes equations with \mathbf{u} , \mathbf{v} denoting the horizontal and vertical component of the velocity respectively while \mathbf{p} denotes the pressure field. The density of the fluid is set to $\rho = 1 \text{ Kg/m}^3$, and dynamic viscosity $\mu = 0.001 \text{ Kg/m s}$. The flow is unsteady with a maximum velocity of 1 m/s and mean velocity $\frac{2}{3}$ of the maximum velocity. The simulation starts with initial conditions $\mathbf{u}_0 = \mathbf{v}_0 = 0$ and $\mathbf{p}_0 = 0$. For the boundary conditions, the leftmost boundary is set as an inlet with a parabolic velocity profile. This is representative of fully developed laminar flow at the inlet. The rightmost boundary is set as an outflow (pressure boundary), where we specify the pressure but do not specify the velocity, allowing the flow to exit naturally based on the internal flow field. All other boundaries are treated as walls with a no-slip condition, which means the fluid velocity at the walls is zero. The simulation runs for a total of 80 seconds, with a time-step size of 0.01 seconds.

Appendix B Network architecture and hyperparameters

The training strategy was already discussed in the main body of the paper. In this section we will mainly go into the details of the network architecture and specific values of the hyper-parameters used for training.

B.1 Network architecture

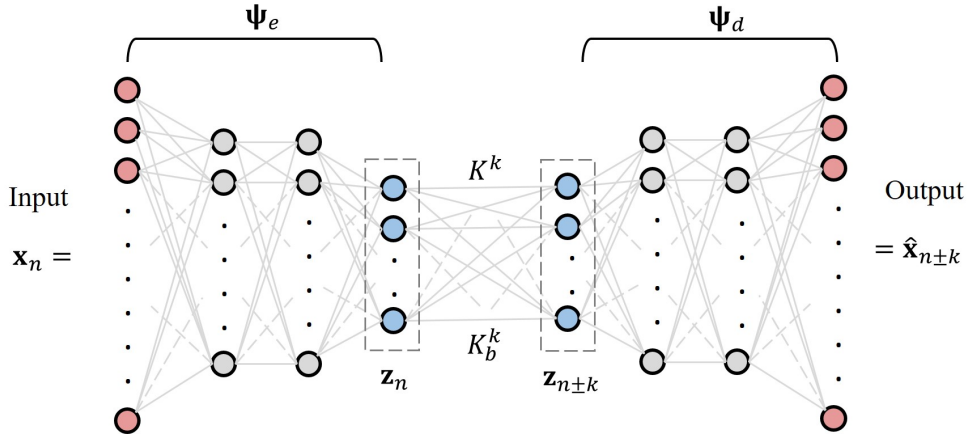


Fig. B3 tcKAE architecture where the layers with red nodes indicate the input and output layer in the original state space. The latent space is represented by the bottleneck layer with blue nodes. The hidden layers are shown by the gray nodes.

The network architecture is shown in Fig. B3. Note that the network topology is same as that in [7]. The number of nodes in the input and output layer (red) is indicated by N_{in} and N_{out} ($N_{\text{in}} = N_{\text{out}}$). N_l denotes the number of nodes in the bottleneck layer (blue), which represents the approximation of Koopman-invariant latent space. Number of nodes in each hidden layers (two hidden layers for each encoder and decoder) is represented by N_h (gray nodes). We keep N_h same for both the hidden layers and it is tuned in multiple of 8 for the pendulum case and in multiple of 16 for plasma beam and fluid flow case. We use the \tanh activation function for each layer except the bottleneck layer.

B.2 Training details

The crucial hyperparameters to tune are learning rate (l_r), learning rate decay rate (l_{rd}), corresponding decay schedule, maximum look-ahead step κ_m , the weights of the individual component of the total loss, i.e. γ_{id} , γ_{fwd} , γ_{bwd} , γ_{con} and γ_{pc} . Among structural hyperparameters, N_h , N_l are crucial. Note that as mentioned in the previous subsection, N_h is varied by varying α . We provide values of these hyperparameters for extreme scenarios for each of the test-case. Note that $N_{\text{in}} = N_{\text{out}}$ are not tunable, and depend on the dimension of the input

data. The pendulum cases is trained for 600 epochs whereas electron beam and fluid flow cases are trained for 1000 epochs.

B.2.1 Oscillating electron beam

Please see Table B1. The learning rate decay schedule for oscillating electron beam is [30, 200, 400, 700], i.e. learning rate is reduced by a factor of 0.5 at epochs 30,70, 200 and 700.

Table B1 Training hyperparameters of DAE, cKAE, and tcKAE for oscillating electron beam

	Method	$N_{in} = N_{out}$	N_h	N_l	l_r	l_{rd}	κ_m	γ_{fwd}	γ_{bwd}	γ_{con}	γ_{tc}	κ_{pm}	e_s
$N_{train} = 40,$ clean	DAE	2447	256	48	1e-3	0.5	10	0.5	-	-	-	-	-
	cKAE	2447	256	48	1e-3	0.5	10	0.5	1e-3	1e-5	-	-	-
	tcKAE	2447	256	48	1e-3	0.5	10	0.5	1e-3	1e-5	1e-1	45	600
$N_{train} = 100,$ clean	DAE	2447	256	32	1e-3	0.5	25	0.01	-	-	-	-	-
	cKAE	2447	256	32	1e-3	0.5	25	0.05	1e-1	1e-5	-	-	-
	tcKAE	2447	256	32	1e-3	0.5	25	0.05	1e-1	1e-5	1e-3	15	600
$N_{train} = 100,$ 30 dB noise	DAE	2447	256	32	1e-3	0.5	25	0.01	-	-	-	-	-
	cKAE	2447	256	32	1e-3	0.5	25	0.1	1e-1	1e-5	-	-	-
	tcKAE	2447	256	32	1e-3	0.5	25	0.05	1e-1	1e-5	1e-2	10	600

B.3 Flow past cylinder

Please see Table B2. The learning rate decay schedule (epochs) is [30, 200, 400, 700] by a factor of 0.5 .

Table B2 Training hyperparameters of DAE, cKAE, and tcKAE for flow past cylinder

	Method	$N_{in} = N_{out}$	N_h	N_l	l_r	l_{rd}	κ_m	γ_{fwd}	γ_{bwd}	γ_{con}	γ_{tc}	κ_{pm}	e_s
$N_{train} = 40,$ clean	DAE	2647	256	64	1e-3	0.5	15	1e-2	-	-	-	-	-
	cKAE	2647	256	48	1e-3	0.5	15	1e-4	1e-6	1e-4	-	-	-
	tcKAE	2647	256	48	1e-3	0.5	10	0.5	1e-3	1e-5	1e-3	50	100
$N_{train} = 100,$ clean	DAE	2647	256	64	1e-3	0.05	15	0.05	-	-	-	-	-
	cKAE	2647	256	48	1e-3	0.5	15	0.05	1e-4	1e-4	-	-	-
	tcKAE	2647	256	48	1e-3	0.5	10	0.05	1e-3	1e-5	1e-3	20	400
$N_{train} = 120,$ 30 dB noise	DAE	2647	256	64	1e-3	0.5	15	2	-	-	-	-	-
	cKAE	2647	256	48	1e-3	0.5	15	0.5	1e-6	1e-4	-	-	-
	tcKAE	2647	256	48	1e-3	0.5	10	0.5	1e-3	1e-5	1e-3	20	100

Appendix C Ablation study

Note that the weights γ_{id} and γ_{fwd} are absolute essential The ablation study essentially contains one extra case where we do not consider the loss components pertaining to backward dynamics, by chosing $\gamma_{bwd} = \gamma_{con} = 0$. The ablation studies are done for the extreme cases. We take the best case for DAE and change the γ_{pc} to obtain optimum result.

Table C3 Ablation study for undamped pendulum

	γ_{id}	γ_{fwd}	γ_{bwd}	γ_{con}	γ_{pc}	Average relative error(%)
$N_{train} = 32$, clean	1	1	0	0	0	26.73
	1	1	0	0	1	02.70
	1	0.5	1e-2	1e-1	0	09.684
	1	0.5	1e-2	1e-1	1e-1	02.93
$N_{train} = 90$, clean	1	0.5	0	0	0	11.29
	1	0.5	0	0	1e-4	7
	1	0.05	1e-4	1e0	0	4.58
	1	0.05	1e-4	1e0	1e-2	3.06
$N_{train} = 90$, 30 dB noise	1	0.01	0	0	0	11.4657
	1	0.01	0	0	1e-2	5.8483
	1	0.01	1e-4	1e-2	0	7.6836
	1	0.01	1e-4	1e-2	1e-4	6.1037

Table C4 Ablation study for oscillating electron/plasma beam

	γ_{id}	γ_{fwd}	γ_{bwd}	γ_{con}	γ_{pc}	Average relative error(%)
$N_{train} = 40$, clean	1	0.5	0	0	0	7.7134
	1	0.5	0	0	1e-1	3.0843
	1	0.5	1e-3	1e-5	0	7.5587
	1	0.5	1e-3	1e-5	1e-1	2.8021
$N_{train} = 100$, clean	1	0.01	0	0	0	0.7706
	1	0.01	0	0	1e-3	0.7251
	1	0.05	1e-1	1e-5	0	0.8110
	1	0.05	1e-1	1e-5	1e-3	0.8025
$N_{train} = 100$, 30 dB noise	1	0.01	0	0	0	3.8473
	1	0.01	0	0	1e-2	3.5740
	1	0.1	1e-1	1e-5	0	3.6404
	1	0.1	1e-1	1e-5	1e-2	3.5597

Table C5 Ablation study for flow past cylinder

	γ_{id}	γ_{fwd}	γ_{bwd}	γ_{con}	γ_{pc}	Average relative error(%)
$N_{train} = 40$, clean	1	1e-2	0	0	0	1.4047
	1	1e-2	0	0	1e-3	1.1124
	1	1e-4	1e-6	1e-4	0	2.22
	1	1e-4	1e-6	1e-4	1e-3	1.1615
$N_{train} = 120$, clean	1	0.05	0	0	0	0.062
	1	0.05	0	0	1e-2	0.061
	1	0.05	1e-3	1e-2	0	0.0637
	1	0.05	1e-3	1e-2	1e-3	0.0613
$N_{train} = 120$, 30 dB noise	1	2	0	0	0	3.211
	1	2	0	0	1e-2	1.8703
	1	0.5	1e-4	1e-4	0	9.4887
	1	0.5	1e-4	1e-4	1e-2	1.7453

References

- [1] Azencot (2020) code. url = <https://github.com/erichson/koopmanAE>.
- [2] Noaa sst data. <https://psl.noaa.gov/data/gridded/data.noaa.oisst.v2.highres.html>.
- [3] Martin Arjovsky, Amar Shah, and Yoshua Bengio. Unitary evolution recurrent neural networks. In Maria Florina Balcan and Kilian Q. Weinberger, editors, *Proceedings of The 33rd International Conference on Machine Learning*, volume 48 of *Proceedings of Machine Learning Research*, pages 1120–1128, New York, New York, USA, 20–22 Jun 2016. PMLR.
- [4] Alex Aussem. Dynamical recurrent neural networks towards prediction and modeling of dynamical systems. *Neurocomputing*, 28(1-3):207–232, 1999.
- [5] A. M. Avila and I. Mezić. Data-driven analysis and forecasting of highway traffic dynamics. *Nature Communications*, 11(1):2090, 2020.
- [6] Bahar Azari and Deniz Erdogmus. Equivariant deep dynamical model for motion prediction. In *International Conference on Artificial Intelligence and Statistics*, pages 11655–11668. PMLR, 2022.
- [7] Omri Azencot, N Benjamin Erichson, Vanessa Lin, and Michael Mahoney. Forecasting sequential data using consistent koopman autoencoders. In *International Conference on Machine Learning*, pages 475–485. PMLR, 2020.
- [8] Coryn A L Bailer-Jones, David J C MacKay, and Philip J Withers. A recurrent neural network for modelling dynamical systems. *Network: Computation in Neural Systems*, 9(4):531–547, 1998. PMID: 10221578.
- [9] Y. Bengio, P. Simard, and P. Frasconi. Learning long-term dependencies with gradient descent is difficult. *IEEE Transactions on Neural Networks*, 5(2):157–166, 1994.
- [10] Oumayma Bounou, Jean Ponce, and Justin Carpentier. Online learning and control of dynamical systems from sensory input. In *NeurIPS 2021-Thirty-fifth Conference on Neural Information Processing Systems Year*, 2021.
- [11] Bo Chang, Minmin Chen, Eldad Haber, and Ed H Chi. Antisymmetricrnn: A dynamical system view on recurrent neural networks. *arXiv preprint arXiv:1902.09689*, 2019.
- [12] Zhengdao Chen, Jianyu Zhang, Martin Arjovsky, and Léon Bottou. Symplectic recurrent neural networks. In *International Conference on Learning Representations*, 2020.
- [13] Junyoung Chung, Caglar Gulcehre, KyungHyun Cho, and Yoshua Bengio. Empirical evaluation of gated recurrent neural networks on sequence modeling. *arXiv preprint arXiv:1412.3555*, 2014.
- [14] Akshunna S. Dogra and William Redman. Optimizing neural networks via koopman operator theory. In H. Larochelle, M. Ranzato, R. Hadsell, M.F. Balcan, and H. Lin, editors, *Advances in Neural Information Processing Systems*, volume 33, pages 2087–2097. Curran Associates, Inc., 2020.
- [15] Erik Englesson and Hossein Azizpour. Consistency regularization can improve robustness to label noise. *CoRR*, abs/2110.01242, 2021.
- [16] Yue Fan, Anna Kukleva, Dengxin Dai, and Bernt Schiele. Revisiting consistency regularization for semi-supervised learning. *International Journal of Computer Vision*, 131(3):626–643, 2023.
- [17] D. Goswami and D. A. Paley. Global bilinearization and controllability of control-affine nonlinear systems: A Koopman spectral approach. In *2017 IEEE 56th Annual Conference on Decision and Control*, pages 6107–6112, Dec 2017.
- [18] Debdipta Goswami and Derek A. Paley. Bilinearization, reachability, and optimal control of control-affine nonlinear systems: A koopman spectral approach. *IEEE Transactions on Automatic Control*, 67(6):2715–2728, 2022.
- [19] Samuel Greydanus, Misko Dzamba, and Jason Yosinski. Hamiltonian neural networks. *Advances in neural information processing systems*, 32, 2019.

- [20] Sepp Hochreiter and Jürgen Schmidhuber. Long short-term memory. *Neural computation*, 9(8):1735–1780, 1997.
- [21] Boyin Huang, Chunying Liu, Viva Banzon, Eric Freeman, Garrett Graham, Bill Hankins, Tom Smith, and Huai-Min Zhang. Improvements of the daily optimum interpolation sea surface temperature (doisst) version 2.1. *Journal of Climate*, 34(8):2923–2939, 2021.
- [22] Xiaowei Jia, Jared Willard, Anuj Karpatne, Jordan Read, Jacob Zwart, Michael Steinbach, and Vipin Kumar. *Physics Guided RNNs for Modeling Dynamical Systems: A Case Study in Simulating Lake Temperature Profiles*, pages 558–566.
- [23] Giancarlo Kerg, Kyle Goyette, Maximilian Puelma Touzel, Gauthier Gidel, Eugene Vorontsov, Yoshua Bengio, and Guillaume Lajoie. Non-normal recurrent neural network (nnrnn): learning long time dependencies while improving expressivity with transient dynamics. In H. Wallach, H. Larochelle, A. Beygelzimer, F. d'Alché-Buc, E. Fox, and R. Garnett, editors, *Advances in Neural Information Processing Systems*, volume 32. Curran Associates, Inc., 2019.
- [24] Giancarlo Kerg, Kyle Goyette, Maximilian Puelma Touzel, Gauthier Gidel, Eugene Vorontsov, Yoshua Bengio, and Guillaume Lajoie. Non-normal recurrent neural network (nnrnn): learning long time dependencies while improving expressivity with transient dynamics. *Advances in neural information processing systems*, 32, 2019.
- [25] B. O. Koopman. Hamiltonian systems and transformation in Hilbert space. *Proceedings of National Academy of Sciences*, 17:315–318, 1931.
- [26] Henning Lange, Steven L Brunton, and J Nathan Kutz. From fourier to koopman: Spectral methods for long-term time series prediction. *The Journal of Machine Learning Research*, 22(1):1881–1918, 2021.
- [27] Bethany Lusch, J Nathan Kutz, and Steven L Brunton. Deep learning for universal linear embeddings of nonlinear dynamics. *Nature communications*, 9(1):4950, 2018.
- [28] A. Mauroy and I. Mezić. Global stability analysis using the eigenfunctions of the Koopman operator. *IEEE Transactions on Automatic Control*, 61(11):3356–3369, Nov 2016.
- [29] John Miller and Moritz Hardt. Stable recurrent models. In *International Conference on Learning Representations*, 2019.
- [30] D. Na, H. Moon, Y. A. Omelchenko, and F. L. Teixeira. Local, explicit, and charge-conserving electromagnetic particle-in-cell algorithm on unstructured grids. *IEEE Transactions on Plasma Science*, 44(8):1353–1362, 2016.
- [31] Sriram S. K. S. Narayanan, Duvan Tellez-Castro, Sarang Sutavani, and Umesh Vaidya. Se(3) koopman-mpc: Data-driven learning and control of quadrotor uavs, 2023.
- [32] Indranil Nayak, Fernando L Teixeira, and Mrinal Kumar. Koopman autoencoder architecture for current density modeling in kinetic plasma simulations. In *2021 International Applied Computational Electromagnetics Society Symposium (ACES)*, pages 1–3. IEEE, 2021.
- [33] Masamichi Ohba and Hiroaki Ueda. An impact of sst anomalies in the indian ocean in acceleration of the el niño to la niña transition. *Journal of the Meteorological Society of Japan. Ser. II*, 85(3):335–348, 2007.
- [34] Samuel E Otto and Clarence W Rowley. Linearly recurrent autoencoder networks for learning dynamics. *SIAM Journal on Applied Dynamical Systems*, 18(1):558–593, 2019.
- [35] Sebastian Peitz, Samuel E. Otto, and Clarence W. Rowley. Data-driven model predictive control using interpolated Koopman generators. *SIAM Journal on Applied Dynamical Systems*, 19(3):2162–2193, 2020.
- [36] Clarence W. Rowley, Igor Mezić, Shervin Bagheri, Philipp Schlatter, and Dan S. Henningson. Spectral analysis of nonlinear flows. *Journal of Fluid Mechanics*, 641:115–127, 2009.

- [37] Mehdi Sajjadi, Mehran Javanmardi, and Tolga Tasdizen. Regularization with stochastic transformations and perturbations for deep semi-supervised learning. In D. Lee, M. Sugiyama, U. Luxburg, I. Guyon, and R. Garnett, editors, *Advances in Neural Information Processing Systems*, volume 29. Curran Associates, Inc., 2016.
- [38] Peter J. Schmid. Dynamic mode decomposition of numerical and experimental data. *Journal of Fluid Mechanics*, 656:5–28, 2010.
- [39] David Sussillo and Omri Barak. Opening the Black Box: Low-Dimensional Dynamics in High-Dimensional Recurrent Neural Networks. *Neural Computation*, 25(3):626–649, 03 2013.
- [40] Naoya Takeishi, Yoshinobu Kawahara, and Takehisa Yairi. Learning koopman invariant subspaces for dynamic mode decomposition. *Advances in neural information processing systems*, 30, 2017.
- [41] Matthew O. Williams, Maziar S. Hemati, Scott T. M. Dawson, Ioannis G. Kevrekidis, and Clarence W. Rowley. Extending data-driven Koopman analysis to actuated systems. *IFAC-PapersOnLine*, 49(18):704–709, 2016.
- [42] Matthew O. Williams, Ioannis G. Kevrekidis, and Clarence W. Rowley. A data-driven approximation of the Koopman operator: extending Dynamic Mode Decomposition. *Journal of Nonlinear Science*, 25(6):1307–1346, Dec 2015.
- [43] Enoch Yeung, Soumya Kundu, and Nathan Hodas. Learning deep neural network representations for koopman operators of nonlinear dynamical systems. In *2019 American Control Conference (ACC)*, pages 4832–4839, 2019.